Blast response of concrete encased carbon composite H-beam columns

Matthew Troemner[a,e,*], Photios Papados[b], Erol Lale[c], Roozbeh Rezakhani[d], Gianluca Cusatis[e]

[a] *Cusatis Computational Services Inc., Wilmette, IL 60091, U.S.*
[b] *Department of Defense, Arlington, Virginia, U.S.*
[c] *Istanbul Technical University, Civil Engineering Department, 34469 Maslak/Istanbul, Turkey*
[d] *Duke University, Department of Civil and Environmental Engineering, Durham, NC 27708, U.S.*
[e] *Northwestern University, Department of Civil and Environmental Engineering, Evanston, IL 60208, U.S.*

Abstract

The response of concrete columns is highly dependent upon their internal reinforcement configuration when subjected to a short duration and high intensity loading, such as one resulting from a detonation event. In recent times, structural engineers have pursued concrete column designs featuring encased steel and/or composite laminate H-beams, as an alternative to traditional longitudinal and transverse (shear) steel reinforcement. Encased beam reinforcement alters shock wave propagation characteristics in the through-thickness direction of the structural element, thus resulting in unique failure phenomena when compared to traditional columns of equivalent quasi-static strength. In this study, the Lattice Discrete Particle Model (LDPM) is initially reformulated for detonation events, implemented in a commercial finite element solver, and validated using experimental data. The model is then employed to investigate the dynamic behavior of three concrete columns with differing internal structures: traditionally reinforced with 25-millimeter Grade 60 rebar, encased A992 steel H-beam, and encased carbon fiber composite laminate H-beam. LDPM is formulated to simulate concrete at the mesoscale – the length scale of the coarse aggregate used in concrete mixtures. Composed of polyhedral cells connected through a lattice of nonlinear fracturing struts, LDPM accurately and precisely captures the failure behavior at the mesoscale level. For this study, a typical 40-MPa concrete is used for all LDPM concrete material input. Linear beam elements with displacement degrees-of-freedom tied to LDPM nodes are used to model embedded rebar, whereas shell elements are employed to simulate the encased sections. The columns are subjected to two ranges of blast loads simulated via realistic pressure distributions along the column height and on all four exposed vertical surfaces. A comparison of the overall column performance is provided through quantitative analysis of mid-span responses as well as qualitative comparison of the overall failure modes. Results show that the encased beam column design provides a significant improvement with respect to the dynamic, post failure performance compared to that of the traditionally reinforced concrete column design.

Keywords: Lattice Discrete Particle Model, Dynamics, Fracture, Concrete, Composite

1. Introduction

Frequently associated with the battlefield abroad, facilities designed with risk mitigation strategies for detonation events are becoming ever more commonplace for high-value government and civilian structures at home. Such building components are traditionally composed of hardened elements - massive reinforced concrete columns, walls, and other structural members purposed to reflect and absorb energy from air blast events, while also providing shielding to occupants and equipment from airborne debris. In new construction, where physical footprint and material usage may not pose an issue, over-strengthening design approaches are often sufficient, provided they meet all other client requirements. In instances of hardening existing infrastructure, spatial or load-bearing constraints may limit the addition of massive reinforced concrete elements, thereby necessitating the use of novel approaches to achieve risk mitigation.

New materials and design techniques exist in the literature with excellent energy absorption capabilities - such as bio-inspired components, graded structures, auxetic materials, reinforced polymers, fibrous materials, and various metamaterials [1, 2, 3, 4, 5, 6, 7, 8, 9]. These advances should not be discounted; however, until widely adopted in construction practice, such technologies pose limited use for the current practitioner. Thus, it is desired to examine the range from typical to state-of-the-art readily-available techniques for detonation hazard mitigation, as it relates to the design of supporting column structures.

As mentioned, the historically typical technique when designing for blast mitigation is to implement massive reinforced concrete components. In the context of columns, this pertains to standard or high performance concrete

*Corresponding author
Email address: mtroemner@u.northwestern.edu (Matthew Troemner)

with embedded steel reinforcing bars, typically of mild grade. When spatial restrictions are of concern, or additional resistance is required, then either embedded steel members [10, 11] or steel jackets [12, 13] may be utilized in conjunction with, or in place of, steel reinforcing bars. Use of these two construction techniques have often proved sufficient; however, in cases of retrofit the added mass of encased or jacketed steel may be excessive, while merely enhancing the reinforcement may be insufficient. In recent times, a novel approach to address this concern has been the introduction of encased carbon fiber laminated composite members, in place of steel encased members, due to superior weight-to-stiffness and weight-to-strength ratios. As an example, a typical anisotropic carbon-epoxy composite, AS4 3501-6/epoxy, has longitudinal elastic modulus and ultimate tensile strength of 126 GPa and 1,950 MPa, respectively, while exhibiting a density of 1.6 g/cm^3 [14, 15, 16], compared to the ASTM A992 steel with elastic and ultimate moduli of 200 GPa and 450 MPa, respectively, but a density of 7.85 g/cm^3 [17] – nearly five times heavier than that of the AS4 composite.

In order to compare performance of columns under explosive loading, three equally-sized columns with different reinforcement techniques were designed. The first reinforcement technique included a traditional reinforcing scheme of longitudinal bars with tied stirrups. The second reinforcement scheme uses the same rebar and stirrup configuration, but also included an encased steel H-beam. The third comparison used a similar internal geometry; however the H-beam was composed of a carbon fiber composite laminate.

2. Detonations and Blast Wave Propagation

An often frequent approach to deliberate bombing attacks is the use of improvised explosive devices (IED) [18] in the form of vehicle bombs, such as the World Trade Center Bombing in 1993 [19], Oklahoma City Bombing in 1995 [20, 21], Stockholm Bombings in 2010 [22], the attempted Times Square Bombing in 2010 [23], and the Norway Attacks of 2011 [24]. In such situations, a vehicle carrying explosive material may be parked adjacent or inside a structure of concern, or even driven into the structure at a high rate of speed. In the wake of the World Trade Center bombings in 1993, many such structures introduced new restrictive measures on interior parking facilities, including access control, vehicle inspections, and more. Further, with the rise of deliberate high-speed forceful vehicle entries, such as the 2017 Stockholm and New York City attacks [25], an increasing level of high-value infrastructure has been introduced or is being erected with vehicle blockades – typically in the form of bollards, concrete planters, or other large structurally-reinforced elements. While such facilities may be shielded from interior parking and high-speed vehicle attacks, many are located in urban areas with little perimeter standoff, and thus remain vulnerable to building-adjacent or on-street detonations.

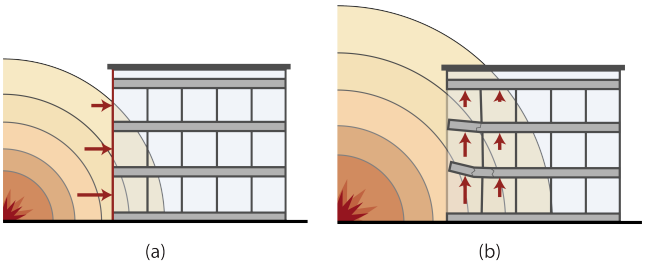

Figure 1: Depiction of advancing blast front from ground-based detonation (a) impacting structure and exerting horizontal force on incident surface; (b) propagating through structure and exerting vertical uplift forces on interior slabs; adapted from FEMA 426 [21].

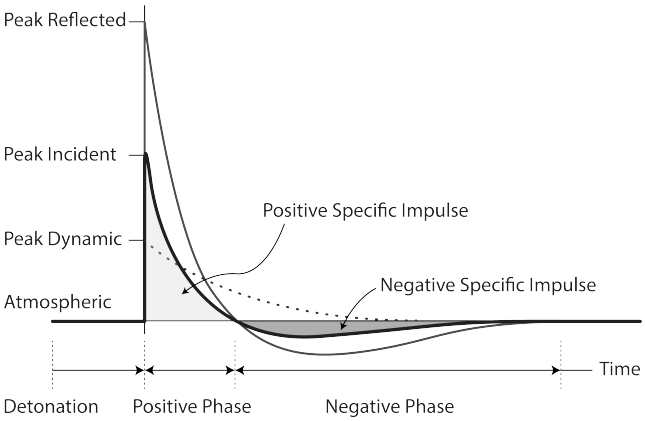

Figure 2: Idealized pressure-time history for an exterior detonation event – exhibiting initial peak pressures, decay to atmospheric pressure, period of negative pressure phase, and return to ambient conditions.

In the cases of vehicle explosions – directly on-street or in neighboring parking and with little standoff – the detonation can be approximated as a ground-bourne hemispherical surface burst. Given the proximity, exterior first floor facade and columns experience the greatest blast pressure (see Figure 1a). Depending on the standoff distance, such loading on the incident surface may either be regarded as a planar uniform load, or as a gradual degrading load with the most significant pressure near ground, vertically aligned with the point of detonation. In tandem with this horizontal loading on the column faces, hemispherical near-field blasts will produce a primarily upward pressure on low-level slab surfaces, permitting vertical displacement of the columns and damage in the slabs (see Figure 1b).

As with all detonations, a supersonic blast front initially impacts the incident surface, typically inducing the most substantial portion of damage. As shown on the pressure-time curve in Figure 2, following contact this positive pressure will decay to the atmospheric air pressure, where it continues decreasing to a negative pressure phase, due to the partial vacuum created by over-expansion in the affected air before it returns to the ambient atmospheric pressure [26].

When a short duration high-intensity loading impacts

the concrete surface, high-speed compression stress waves develop at the incident surface and are transmitted through the medium. These waves interact with heterogeneous inclusions, such as the reinforcement, and are, subsequently, both reflected at the concrete-reinforcement interface and partially transmitted through the new medium. Within the reinforcement, stress waves travel at differing velocities from those of the surrounding concrete. Such behavior results in internal stress concentrations due to differing wave arrival times in the cross section, further exacerbating interfacial failure planes. When the compression waves reach the rear surface of the structure, they are reflected as tensile waves and also induce a longitudinal stress perpendicular to the direction of the wave propagation (i.e. vertical stress in horizontally-loaded columns) [27]. While reinforcement can certainly increase overall concrete strength, such phenomena ensure that the physical response under a short duration intensive loading is highly dependent on the internal reinforcement configuration.

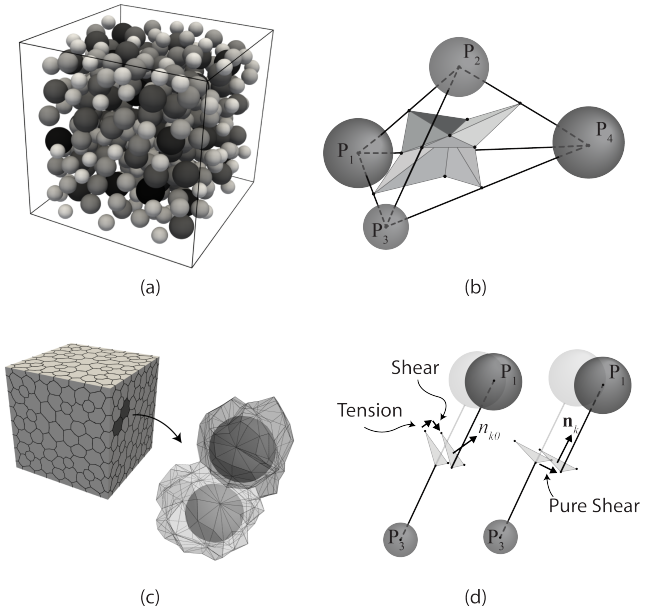

Figure 3: (a) LDPM particles in a cubic geometry following placement procedure; (b) set of four LDPM particles and associated facets; (c) set of two LDPM polyhedral cells composed of a single particle and their surrounding facets; (d) set of two facets interacting in tension-shear and pure shear. Distances are exaggerated for clarity.

3. Modeling of Reinforced Concrete

In this study, the Lattice Discrete Particle Model (LDPM) [28, 29] was adopted to model the bulk concrete material due to extensive validation and testing of fracturing behavior [30, 31, 32, 33], suitability for reinforcement inclusion [34, 35], and application to impact and blast loads [36, 37, 38, 39, 40]. Reinforcing bars and plates were modeled with the Finite Element Method (FEM) due to extensive existing material libraries [41] and ease of material performance comparisons. Embedded/encased reinforcement was modeled with appropriate failure and damage criterion for the material, and translation bonds with concrete were assumed to be perfect.

3.1. Lattice Discrete Particle Model

LDPM is a discrete model which describes the internal structure of concrete via interaction of polyhedral cells connected through a lattice framework of nonlinear fracturing struts. Operating at the mesoscale, or the scale of aggregate, these polyhedral cells each represent a single aggregate particle surrounded by a layer of mortar. By design, the cellular mesh is heterogeneous, with each cell unique in shape and correlated to a probability density function based on real aggregate size distribution. The cells are conformal with the coincident surface facets, permitting development of unique connecting struts – where the constitutive equations are imposed and fracturing is permitted.

The cellular mesh is developed through a detailed discretization procedure outlined in Cusatis et al. [28]. In brief: utilizing water-to-cement ratio, cement content, maximum and minimum particle size, and sieve curve, the number and size distribution of required particles can be calculated. These particles are placed in the desired geometry through a trial-and-error approach, under requirements for no overlaps, minimum offsets, and no external surface intersections (Figure 3a). A compatible mesh size is then used to generate particles of zero-radius on the geometry surface for development of the skeletal lattice system. Using both particle sets, a Delaunay tetrahedralization of the entire volume is performed on the particle centers. Following tetrahedralization, a dual tessellation procedure is performed on the tetrahedron edges and faces, such that each tetrahedron is subdivided by 12 triangular bisecting facets (Figure 3b). All facets associated with a given particle are combined to create the surface of the polyhedral cells (Figure 3c).

The interaction of the polyhedral cells in LDPM operate within rigid body kinematics – where all facets of a given cell are constrained to a single rigid body point. Rigid body kinematics allows calculating by displacement jumps at the interface between adjacent cells, $[\![\mathbf{u}]\!]^{IJ}$. To avoid non-symmetric behavior in pure shear, these interactions are defined in a projected facet system of reference where the projection is in a plane orthogonal to the associated tetrahedron edge [28, 42]. These displacement jumps are used to define facet strains, as shown in Equation 1:

$$\mathbf{e} = l^{-1}\mathbf{P}^{IJ}[\![\mathbf{u}]\!]^{IJ} \tag{1}$$

where $[\![\mathbf{u}]\!]^{IJ} = \mathbf{u}^J + \boldsymbol{\varphi}^J \times \mathbf{c}^J - \mathbf{u}^I - \boldsymbol{\varphi}^I \times \mathbf{c}^I$, l is the tetrahedron edge length, $\mathbf{P}$ defines the appropriate unit vector directions, $\mathbf{u}$ and $\boldsymbol{\varphi}$ are displacement and rotation, and $\mathbf{c}^I$ and $\mathbf{c}^J$ are vectors connecting the centers of the I and J cells with the centroid of the interface facet [36].

LDPM assumes a linear relation for stress and strain in the elastic regime, which can be defined as $t_N = E_0 e_N$, $t_M = E_T e_M$, and $t_L = E_T e_L$, where $E_T = \alpha E_0$, and

E_0 and α are the material parameters for effective normal modulus and shear-normal coupling. Beyond the elastic regime, three distinct mechanisms govern the mesoscale nonlinear behavior:

Compression: Compaction and Pore Collapse. Under compressive loads, $e_N < 0$, concrete behavior is characterized by pore collapse and pore-wall interactions, which result in strain-hardening plasticity and significant material densification [43]. LDPM simulates this phenomenon with a facet-level strain-dependent compressive normal stress boundary, σ_{bc}, which is a function of the volumetric strain of the tetrahedron (Figure 3c), $e_V = \Delta V/3V_0$, and the deviatoric strain, e_D, where the latter is calculated as $e_D = e_N - e_V$ [28]. In this context, LDPM regards σ_{bc} as the result of the piecewise function given by the Equation 2, and must satisfy $-\sigma_{bc} \leq t_N \leq 0$.

$$\sigma_{bc} = \begin{cases} \sigma_{c0} + H_c \langle -e_V - e_{c0} \rangle, & -e_V \leq e_{c1} \\ \sigma_{c1} \exp\left[H_c \left(-e_V - e_{c1}\right)/\sigma_{c1}\right], & \text{otherwise} \end{cases} \tag{2}$$

where σ_{c0} is the mesoscale compressive yield stress, $e_{c0} = \sigma_{c0}/E_0$ is the compaction strain at the start of pore collapse, $e_{c1} = \kappa_{c0} e_{c0}$ is the compaction strain at the start of rehardening, κ_{c0} is a material parameter, $\sigma_{c1} = \sigma_{c0} + H_c \left(e_{c1} - e_{c0}\right)$. H_c is the initial hardening modulus calculated as: $H_c = H_{c1} + (H_{c0} - H_{c1})/(1 + \kappa_{c2} \langle r_{DV} - \kappa_{c1} \rangle)$, where H_{c0}, H_{c1}, κ_{c1}, and κ_{c2} are material parameters, and r_{DV} is the deviatoric-to-volumetric strain ratio. When $e_D \leq 0$ then $r_{DV} = |e_D|/(e_{V0} - e_V)$, otherwise $r_{DV} = |e_D|/e_{V0}$, where $e_{V0} = 0.1 e_{c0}$. Note that all instances of $\langle . \rangle$ notation are used as Macaulay brackets to describe a ramp function. Under unloading/reloading in a compacted state, $-t_N > \sigma_{c0}$, concrete features an incremental elastic behavior that is stiffer than the initial elastic behavior. This is captured by calculating the normal stress increments during unloading/reloading as $t_N = E_d e_N$, where $E_d > E_0$ is the densified normal modulus.

Compression-Shear: Frictional Behavior. Frictional behavior in LDPM is characterized by correlating shear strength to compressive stresses. With increased levels of compression, the shear strength of a facet will be increased to account for microscale frictional effects. Classical incremental plasticity is used for the frictional implementation in LDPM. Shear stress increments are calculated as $\dot{t}_M = E_T \left(\dot{e}_M - \dot{e}_M^p\right)$ and $\dot{t}_L = E_T \left(\dot{e}_L - \dot{e}_L^p\right)$, where $\dot{e}_M^p = \dot{\lambda} \partial \psi / \partial t_M$ and $\dot{e}_L^p = \dot{\lambda} \partial \psi / \partial t_L$. φ is the plastic potential: $\psi = (t_M^2 + t_L^2)^{1/2} - \sigma_{bs}$, and σ_{bs} is the shear strength boundary as formulated in Equation 3.

$$\sigma_{bs} = \sigma_s + \mu_0 \sigma_{N0} \left[1 - \exp\left(t_N/\sigma_{N0}\right)\right] \tag{3}$$

where σ_{N0} is the transitional normal stress, μ_0 is the initial internal friction coefficient, and σ_s is cohesive shear strength.

Tension and Tension-Shear: Fracture and Cohesion. The final inelastic behavior captured by LDPM is fracture and cohesion through tension and tension-shear. When a facet is in tension, such that $e_N > 0$, normal and shear stresses are calculated as $t_N = e_N \left(t/e\right)$, $t_M = \alpha e_M \left(t/e\right)$, and $t_L = \alpha e_L \left(t/e\right)$, where the effective strain is $e = (e_N^2 + \alpha e_T^2)^{1/2}$, $e_T^2 = e_M^2 + e_L^2$; and the effective stress is $t = t_N^2 + t_T^2/\alpha)^{1/2}$, $t_T^2 = t_M^2 + t_L^2$. In a manner similar to the other behaviors, a strain-dependent boundary is developed for tensile stress, as shown in Equation 4.

$$\sigma_{bt} = \sigma_0 \left(\omega\right) \exp\left[-\frac{H_0 \left(\omega\right)}{\sigma_0 \left(\omega\right)} \left\langle e - e_0 \left(\omega\right) \right\rangle\right] \tag{4}$$

where $e_0 \left(\omega\right) = \sigma_0 \left(\omega\right)/E_0$ is the tensile strain threshold, $H_0 \left(\omega\right) = H_t (2\omega/\pi)^{n_t}$ is the softening modulus, ω is the degree of interaction between shear and normal loading: $\tan\left(\omega\right) = e_N/\sqrt{\alpha} e_T = t_N \sqrt{\alpha}/t_T$, $\sigma_0 \left(\omega\right)$ is the effective strength limit:

$$\sigma_0 \left(\omega\right) = \sigma_t \frac{-\sin\left(\omega\right) + \sqrt{\sin^2\left(\omega\right) + 4\alpha \cos^2\left(\omega\right)/r_{st}^2}}{2\alpha \cos^2\left(\omega\right)/r_{st}^2} \tag{5}$$

where r_{st} is the shear-to-tensile strength ratio: $r_{st} = \sigma_s/\sigma_t$.

3.2. Strain Rate Effect

Concrete dynamic behavior depends on the rate of loading. In the literature, rate effect is typically modeled via the so-called Dynamic Increase Factor (DIF), which is defined as the ratio between the dynamic and quasi-static strength. This approach is not general because it does not distinguish between "intrinsic" phenomena (e.g. creep, thermal activation of fracture processes, presence of capillary water), which should be included in the constitutive equations, and "apparent" phenomena (e.g. inertia effects, crack pattern, delayed localization), which are structural features of the response and should or should not be included in the constitutive equations depending on the spatial and temporal resolution of the adopted computational framework. A detailed review of intrinsic and apparent phenomena with reference to LDPM can be found in Cusatis et Al. [39]. Furthermore, interested readers can find the formulation of the LDPM constitutive equations to account for creep and strain rate dependence of crack processes in Cusatis [38]. Cusatis and collaborators [38, 39] also demonstrated that for high strain rates (¿

3.3. Numerical Handling of Large Deformations for Detonation Events

As mentioned, LDPM has proven suitability for modeling concrete behavior under high strain-rate events [37, 38, 39, 40]; however, all of the existing studies demonstrating this application have been limited to relatively small projectile impacts, spatially confined deformations, or small demonstration samples. In cases of large detonations with significant concrete damage and deformation, like those associated with vehicle bombs, several physical and numerical issues arise in the current formulation of LDPM.

While a discrete model, strains in LDPM are fundamentally formulated on the tetrahedron – a composite of

four distinct particles with potentially differing trajectories during severe concrete damage. As the displacement jump of these polyhedral cells increase, so do the associated facet-level strains. Fracturing criteria are imposed in the existing LDPM formulation, and thus these measures do not alter particle-physics; however, associated matrices and calculations are continually updated, increasing computational cost and sensitivity of already large, intensive models. To reduce this demand, a final failure criterion based on volumetric strain was imposed, which when triggered eliminates most facet-level calculations. For this study, a value of 20% volumetric strain (calculated as $e_V^* = \Delta V/3V_0$) was deemed appropriate to capture a fully-failed facet (this corresponds to a new tetrahedron volume equal to 1.6 times the original volume). After a facet reached the 20% threshold, all force and interaction calculations were seized, and the particle was merely tracked as a free rigid body in space. This method ensured fully-fractured polyhedral cells would not disturb the continuing concrete simulation, while still permitting inclusion of these cells in post-fragmentation analyses.

In large deformation modeling an additional concern is the way strain measures are calculated. In the traditional implementation of LDPM, the facet-level strains (Equation 1) are formulated on the premise of original tetrahedron edge lengths. Although sufficient in situations of relatively small displacements and small rotations, this formulation produces spurious effects in a manner similar to the violation of infinitesimal strain theory under situations of extreme deformation. Thus, for large detonation simulations, the tetrahedron edge lengths were updated at each numerical increment, as shown in Equation 6:

$$l_e^* = \left\|\mathbf{x}_j^* - \mathbf{x}_i^*\right\| = \left[\left(\mathbf{x}_j^* - \mathbf{x}_i^*\right)^{\mathrm{T}}\left(\mathbf{x}_j^* - \mathbf{x}_i^*\right)\right]^{1/2} \quad (6)$$

where $\mathbf{x}^*$ describes the current position of node i or j, and l_e^*.

Finally, there are physical and numerical concerns for large rotations of particles and facets. In the traditional description of LDPM, corotational systems of reference are formulated at the tetrahedron-level. In situations where single particles significantly rotate with respect to the other particles in a given tetrahedron, numerical issues arise for determination of the present system of reference – which may in turn percolate to physical particle behavior. To overcome this potential issue, the updated LDPM implementation used a facet-level formulation for all local coordinate systems.

3.4. LDPM Commercial Solver Implementation

For streamlined simulations and integration with existing finite element and interaction libraries, the Lattice Discrete Particle Model was implemented in the commercial finite element analysis (FEA) solver, Abaqus Unified FEA [44] – note that all discussion of Abaqus in this study and implementation is limited to Abaqus/Explicit. Implementation in Abaqus is performed through a combination of FORTRAN-based user subroutines and an externally-referenced facet data file. Concrete polyhedral mesh structures and corresponding facet data (including facet nodes, normal/tangential components, projections, areas, etc.) are initially produced with an external meshing script. This program follows the same general process described in Cusatis et al. [28], with current implementation further described in Troemner et al. [45]. Along with developing the facet data file, the tetrahedral lattice is constructed for importing into Abaqus. This mesh may be manipulated in the same manner of an Abaqus-native mesh, including imposition of boundary conditions, constraints, interactions, and other features. One inherent limitation is lack of shape functions, due to the discrete nature of the LDPM formulation. In practice, this means all such features must be imposed on the LDPM tetrahedron nodes, rather than edges, surfaces, or volumes.

LDPM is numerically implemented in Abaqus though the 'VUEL' user element subroutine, with cases involving friction also referencing the 'VFRIC' contact friction subroutine [41]. In each increment where information about an LDPM element is required: Abaqus calls the user element subroutine and passes all nodal coordinates, solution dependent variables (displacement, velocity, rotation, etc.), and solution dependent state variables (facet stresses, strains, crack opening, dissipated energy, etc.) for that element. If the simulation is at $t = 0$ then the user element subroutine will call other LDPM-associated subroutines to calculate the mass matrix, stable time increment, tetrahedron volumes, and all other required initial data. If the simulation is at $t > 0$ then the user element subroutine will transfer all solution variables to other LDPM-associated subroutines which perform the calculations in Section 3.1 at the facet-level. Following calculation, all variables are passed back through the facet-level, LDPM-level, and FEA-level subroutines. At the top-most level, Abaqus uses the element mass matrix and load contributions to solve for acceleration at the end of each increment: $\ddot{u}_{(i)}^N = (M^{NJ})^{-1}(P_{(i)}^J - F_{(i)}^J)$, where M^{NJ} is the lumped mass matrix, $F_{(i)}^J$ is the internal force vector, and $P_{(i)}^J$ is the external force vector. This solution is then integrated with the central difference method to obtain the velocity and displacement in Equations 7 and 8 [41].

$$\dot{u}_{(i+1/2)}^N = \dot{u}_{(i-1/2)}^N + \frac{\Delta t_{(i+1)} + \Delta t_{(i)}}{2}\ddot{u}_{(i)}^N \quad (7)$$

$$u_{(i+1)}^N = u_{(i)}^N + \Delta t_{(i+1)}\dot{u}_{(i+1/2)}^N \quad (8)$$

It is worth mentioning that by using the built-in Abaqus subroutines to govern the underlying LDPM calculations, the code is fully parallelized. Thus, any LDPM domains can be decomposed in the same manner as any FEA decomposition.

3.5. Embedded Rebar Reinforcement Model

Given the inability of Euler-Bernoulli beam formulations to capture transverse shear deformation and rota-

tional bending effects, Timoshenko beam elements were used for modeling all reinforcing bars. As such, rebar element cross-sections were assumed to not deform, remain planar, and their transverse shear response was independent of any axial deformation or bending. The rebar elements were of simple linear two-node beam element construction, each node with six degrees of freedom (DOFs) – three translational and three rotational. For simplicity, all elements additionally used a lumped mass matrix formulation. Further, rebar beam element lengths were of 1.5 times the maximum aggregate diameter in the system, as is consistent with past LDPM procedures.

Past studies on reinforced concrete modeled with LDPM have implemented the rebar-concrete bond as a constraint between LDPM tetrahedron volumes and rebar nodes [34, 46]. While such formulation has shown suitability in specific cases, there is the possibility that only one or two may actually reside in the immediate proximity of reinforcing bars. This results in a potential over-constraining effect by unionising four independent particles. Further, such constraints are quite difficult to develop in the current Abaqus implementation, as this would require an FEA lattice recognizable by Abaqus or an additional subroutine to independently handle the constraint. Thus, a kinematic translational constraint formulated on the basis of LDPM nodes and rebar nodes was devised. As shown in Figure 4a, all concrete nodes were provided a tie search radius equal to one-half the average particle-to-particle distance in the LDPM mesh. If any rebar element nodes fell within that search radius then the two nodes were tied together. The kinematic constraint was imposed such that relative translational displacements of the nodes were always zero. Rotations of each node were permissible, so to allow physically-realistic twisting of the bars and small localized rotational deformations. In situations of single nodes acting as the subject of two or more tie constraints, penalty method was employed to resolve such overconstraint behavior.

Finally, all rebar material behavior was governed by the von Mises (J2) yielding criterion and isotropic hardening up to the point of failure. Damage was imposed through a ductile damage model, with damage initiation controlled by strain at fracture, stress triaxiality, and strain rate, and damage evolution a linear displacement-based function. Rate effect was not imposed for the reinforcing bars given limited available data at the considered strain rates.

3.6. Encased Beam Reinforcement Model

Given the large volume associated with encased beams, concrete volumes overlapping these members were removed prior to LDPM mesh generation, creating voids where the H-beams could perfectly fit. All H-beams, both of steel and carbon fiber composite, were modeled with four-node shell finite elements of a size similar to that of the LDPM tetrahedron surface triangles. Despite encasement in a solid geometry, shell elements were selected due to improved bending behavior and concerns over shear and volume locking. Unlike reinforcing bars which used a search radius for determination of tie constraints, the encased beams were formulated such that the theoretical offset surface nodes were directly tied to the nearest LDPM node on the interior void surface (see Figure 4b). Additionally for the encased H-beams ties, all six degrees of freedom were constrained, as rotations at the interface were not expected.

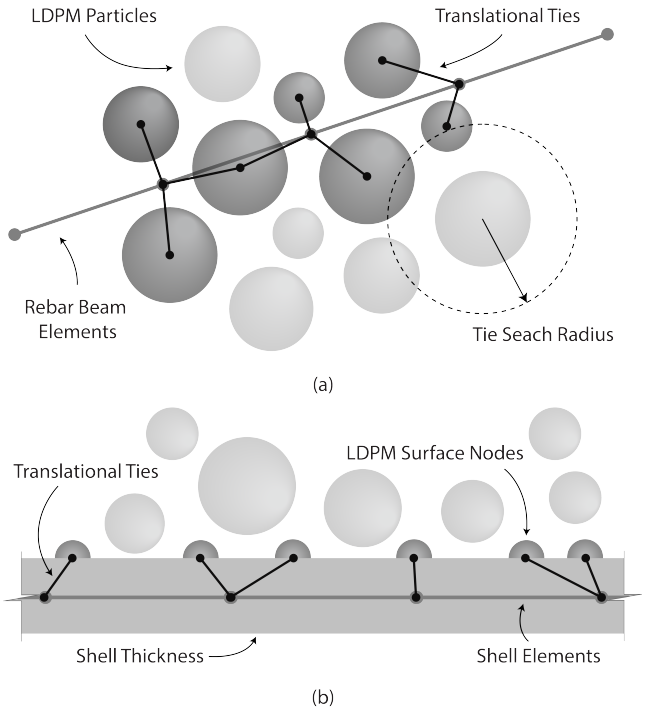

Figure 4: (a) Depiction of rebar-concrete bond constraints and associated tie search radius; (b) depiction of encased members-concrete bond constraints. Light grey LDPM particles are free and dark grey particles are tied. Note that distances are exaggerated for clarity.

Encased Steel Members. The encased steel members were modeled with homogeneous 4-node reduced integration shell elements with five integration points through the thickness. As with the steel reinforcing bars, the encased steel H-beams were governed by J2 plasticity and isotropic hardening. Further, a similar ductile damage model was imposed to simulate potential beam tearing.

Encased Composite Members. The encased carbon fiber members used composite shell elements with one integration point per layup layer, with number of layers dependent on specific section and layer thickness. The elements were characterized by a symmetric quasi-isotropic lamina layup, with constitutive behavior simulated by means of lamina elasticity and the Hashin damage model.

4. Modeling of Air-Blast Detonation Loads

As previously discussed, given LDPM is formulated in a discrete framework, interactions and loads may only be applied to LDPM nodes – not surfaces or edges. Thus, for conditions such as blasts or impacts, another loading

scheme must be developed. For this study, all exterior LDPM surfaces were directly overlaid with three-node planar surface-element meshes, with nodes coinciding external LDPM nodes. Each of these LDPM nodes had all six degrees-of-freedom tied to the coincident surface nodes. Given the surface finite element formulation, load applications were permitted on faces and edges, which were transmitted to LDPM nodes, and at the same time provided no undesired rotational or translational stiffness. With such a surface, blast loads could be imposed through any number of loading schemes, two of the most common being CONWEP and discrete pressure fields.

CONWEP (Conventional Weapons Effect) was developed by the U.S. Army as a set of equations and curves for determination of blast loadings from TM 5-855-1, "Design and Analysis of Hardened Structures to Conventional Weapons Effects" [47, 48]. The CONWEP model in Abaqus uses scaled explosive distances, calculated via a combination of real standoff distance and explosive mass, as expressed via an equivalent quantity of Trinitrotoluene (TNT). The scaled explosive is mapped as a spherical outward-propagating shock wave, which interacts with the surface-element mesh as an incident pressure. Further, CONWEP captures 'real' explosive phenomena, such as the exponential decay of a positive pressure phase, followed by a period of negative pressure [41]. As an empirical model, CONWEP does not require direct simulation of pressure waves traveling through a medium to model air blast effects. Instead, a total pressure is calculated on a specified surface as a function of known incident pressure (P_i), reflected pressure (P_r), and angle of incidence (θ). When $cos\theta \geq 0$ then total pressure is calculated as: $P_t = P_i \left[1 + \cos\theta - 2\cos^2\theta\right] + P_r \cos^2\theta$, otherwise total pressure is equal to incident pressure.

CONWEP models are generally sufficient for small or moderate size basic simulation cases when macroscopic structural behavior is of main concern. In cases of very large blasts or when the concern is phenomena relying on specific blast pressure interactions, such as fragmentation, the smoothed approximations of CONWEP tend to break down. In these latter situations, a common alternative modeling technique is the capture of expected or real surface pressures from computational fluid dynamics (CFD) simulations or experimental data. With pressure-time histories developed at many points over the concrete, the surface-element mesh may be decomposed, with precise loading applied to the specific elements or spatial regions which would experience these pressure histories.

Given the high dependency of structural blast response to strain rate and inertia, simulations including detonation loads are typically modeled in a real-time explicit sense covering the entire pressure-time history. Further, all LDPM simulations which used such loading were simulated over a period of several times the duration of the positive-negative blast phase (Figure 2) to ensure adequate capture of time-delay behavior from inertial effects.

5. Numerical Simulation of Experimental Data

An initial study was developed to verify the appropriateness of the overall LDPM implementation in Abaqus, as well as the selected formulations for blast surfaces, rebar ties, and LDPM formulation updates for detonation events. The experimental dataset in Kumar et al. [49] was selected for direct numerical and qualitative comparison, given a wide range of scaled standoff distances, industry-typical concrete and reinforcing bars, and an included numerical model. In this study, a series of identical concrete slabs were subjected to various blast masses and offset distances, creating six unique scaled blast loadings. Lacking direct pressure data, and given the desire to compare with the provided finite element results, the CONWEP blast implementation method was used.

5.1. Unreinforced Concrete Behavior and Calibration

Sufficient mix design information was provided in Kumar et al. [49] for complete development of an LDPM mesh. This included cement, fine aggregate, coarse aggregate weight ratio of 1:1.66:2.38, a water-to-cement ratio of 0.4, and maximum aggregate size of 10 mm. Further, a Fuller curve coefficient of 0.4 was approximated and a minimum aggregate size of 5 mm ($d_0 = 0.5d_a$, as typical for computational purposes) was assumed.

While comprehensive quantification of concrete mechanical behavior was not present in Kumar et al., invalidating the ability to perform a complete material calibration procedure on the LDPM concrete, the provided 40 MPa compressive strength (46.8 MPa for tested cubes) was sufficient to select a similar already-developed concrete from Cusatis et al. [29]. Given similar compressive strength and concrete purpose (for dynamic applications), the LDPM parameters from the Cusatis et al. Section 5.1 concrete were selected. LDPM cubes and cylinders were generated with model properties from the Kumar et al. mix and with LDPM parameters from Cusatis et al. Section 5.1. These samples were simulated under quasi-static compression loading with high friction plattens, and attained strengths of a similar range to those reported.

5.2. Reinforced Concrete Subjected to Air-Blasts

The experimental setup, consisted of a reinforced concrete slab of 1,000 mm × 1,000 mm × 100 mm resting on two steel supports of equal length with a 100 mm × 150 mm cross section. A Gelatin stick charge was suspended above the slab at a standoff of either 100 mm or 500 mm, and mass of 1.37 kg, 1.62 kg, or 3.25 kg (0.85 kg, 1.0 kg, 2.0 kg equivalent TNT). The steel bar supports were assumed to remain in the linear-regime and thus modeled as linear-elastic material, using traditional reduced integration hexahedral FEA elements. The bottom surfaces on the supports were given encastre (fully-fixed) boundary conditions, constrained from rotation and displacement. The interaction between the concrete and steel support surfaces were modeled as a surface-to-node

hard contact with penalty constraint, and tangential friction with a coefficient of 0.3. Reinforcing bars were specified as 10 mm High Yield Strength Deformed (HYSD) Grade Fe500 (IS 1786:2008), placed in both in-plane directions at 100 mm on-center spacing, and in the middle of the through-thickness direction. They were developed numerically as outlined in Section 3.5, with properties equal to those specified in Kumar et al. [49]: density $\rho = 7,800$ kg/m^3, yield strength $\sigma_y = 609$ MPa, ultimate strength $\sigma_u = 745$ MPa, strain at fracture $\bar{\varepsilon}^{pl}_D = 0.13$, stress triaxiality $\eta = 0.333$, and strain rate $\dot{\bar{\varepsilon}}^{pl} = 2.5 \times 10^{-2}$ s^{-1}. CONWEP was used for imposing blast loads on the slab, through the surface elements previously discussed. A reference point was located in space equal to the location of the hung plastic explosive in the experimental study. The CONWEP blast point was coincident with this reference point, with blast mass equal to the equivalent TNT mass for the explosive. The CONWEP incident surface was selected as the top facing slab surface; no blast interactions were applied to the other concrete surfaces.

Simulations were performed for all six of the scaled blast loads, ensuring each ran for a period equivalent to three times the pressure history curve for capture of inertial effects. Qualitatively the slabs were compared to the experimental results for cracking patterns, fractured rebar, and overall slab behavior. Numerically the simulations were queried for absolute deflection of the bulk slab (excluding ejecta) and blast cone size. A comparison of the cracking patterns for two blast standoff distances (both 1.0 Kg TNT equivalent explosive) are provided in Figure 5, and an excerpt of blast cone size measurement comparisons is provided in Table 1. Both qualitatively and quantitatively the LDPM simulations agreed well with the behavior and responses in the experimental study. Average blast cone sizes were closely reproduced, while measurements parallel and perpendicular to supports were reproduced exceptionally well – in the case of 1.0 Kg TNT equivalent and 100 mm standoff, within 2.1% of experimental values. The diagonal terms encountered slightly greater errors, which was expected as damage would be enhanced and extended to points of larger inclusions, specifically overlapping rebar. This is a phenomenon not captured in the model given that the rebar beam-elements do not disrupt the physical concrete mesh. Such behavior is further evident in the blast cones in Figure 5c and d where the experiment exhibits a more squared-off failure field, compared to a rounder cone in the numerical study.

Table 1: Blast cone size measurements for simulated and experimental slab with 100 mm distance and 1.0 Kg TNT equivalent explosive. Direction measurements correspond to those in Figure 5c, where D11 is parallel to supports, D22 is perpendicular, and D33/D44 are on diagonals.

Direction	Numerical	Experimental [49]	Error
D11	67.4 cm	66.0 cm	2.1%
D22	68.1 cm	68.6 cm	0.7%
D33	72.7 cm	81.3 cm	10.6%
D44	75.4 cm	78.7 cm	4.2%
Average	70.9 cm	73.7 cm	3.8%

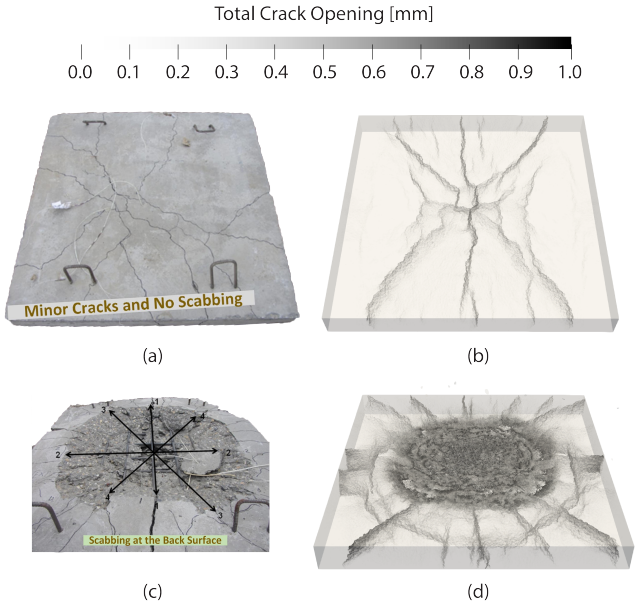

Figure 5: Slab underside of 500 mm standoff distance in (a) experimental study [49], (b) LDPM crack openings. Slab underside of 100 mm standoff distance in (c) experimental study [49], (d) LDPM crack openings. Note that all facets with opening greater than 1 mm (assumed fully disconnected) were removed for clarity.

6. Dynamic Response of Columns with Differing Reinforcement Schemes

As mentioned, structural engineers have recently pursued concrete column designs with encased steel and/or composite laminate H-beams when increased dynamic resistance is required, such as when attempting to mitigate the hazards associated with vehicle-born improvised explosive devices (VBIED). To investigate potential implications of this approach, as well as compare performance of encased steel versus composite beams, models for three concrete columns with differing internal structures were developed: traditionally reinforced with 25 mm Grade 60 rebar and stirrups, encased A992 steel H-beam, and encased carbon fiber composite laminate H-beam. Note that both encased H-beam columns also included longitudinal rebar and stirrups, as is typical in practice. The models were developed to replicate conditions of a first-floor column impacted by near- and far-standoff vehicle explosions. Physical geometry and conditions were developed for a standard mid-rise reinforced concrete structure, and pressure curves were consistent with realistic blast loadings for these types of detonations. Pressures associated with the near-standoff (severe) were approximately one order of magnitude greater than those of the far-standoff (mild) case.

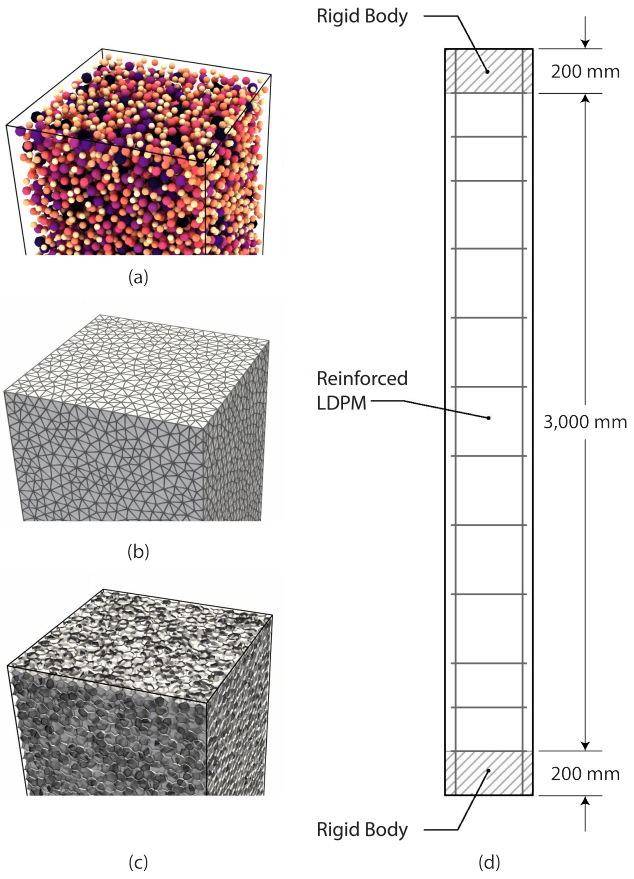

Figure 6: (a) Particles generated for LDPM concrete column mesh; (b) tetrahedralization of column particles; (c) LDPM polyhedral cell facets; (d) schematic of modeled column.

6.1. Numerical Model Development

For this study, columns used a 3 meter free span, with an additional 0.2 meters embedded in a theoretical top and bottom slab, as shown in Figure 6d. The cross section was 400 mm square, and all three columns had four 25 mm longitudinal rebar and ten 10 mm stirrups with 30 mm cover. Exact concrete formulation was not critical as all comparison columns employed the same mix, thus a standard #57 stone was selected for aggregate and all other meshing parameters for the concrete mix were extracted from the Section 5.1 concrete in Cusatis et al. [29]. As such, columns were meshed with the following parameters: cement content $c = 264\,\mathrm{kg/m^3}$, water-to-cement ratio $w/c = 0.553$, concrete density $\rho = 2,290\,\mathrm{kg/m^3}$, maximum aggregate diameter $d_a = 25$ mm, minimum aggregate diameter $d_0 = 12.5$ mm, Fuller curve coefficient $n_f = 0.50$, and volume fraction of entrained air $v_{air} = 0.03$. This resulted in solid LDPM meshes composed of 45,874 cells and 4,008,976 facets (average of three seeds) – columns with encased beams used slightly fewer LDPM cells/facets given the encased beam voids. Additionally, LDPM concrete parameters were again used for the 40-MPa concrete in Cusatis et al. Section 5.1, as outlined in Table 2.

To model the monolithic nature of column-slab embedment, the top and bottom 0.2 meters of LDPM nodes were constrained to rigid-body points located at the center of mass of those 0.2 meter sections, as noted in Figure 6d. The bottom rigid body was fully-fixed in space, to mimic embedment in a ground slab, which would experience little response from a vehicle explosion. The top rigid body was permitted to translate vertically, but had all five other degrees-of-freedom fully constrained. This behavior was selected such to reproduce the potential uplift experienced by upper-floor slabs following ground-based detonations, as depicted in Figure 1b.

Table 2: Values of LDPM parameters governing the concrete mechanical behavior for all columns.

Parameter	Value
Normal modulus, E_0 (MPa)	38,636
Shear-normal coupling, α (-)	0.25
Tensile strength, σ_t (MPa)	4.16
Tensile characteristic length, l_t (mm)	100
Shear-tensile strength ratio, r_{st} (-)	2.7
Softening exponent, n_t (-)	0.2
Compressive strength, σ_{c0} (MPa)	120
Initial hardening modulus ratio, H_{c0}/E_0 (-)	0.67
Final hardening modulus ratio, H_{c1}/E_0 (-)	0.1
Transitional strain ratio, κ_{c0} (-)	3.8
Deviatoric strain ratio, κ_{c1} (-)	1.2
Deviatoric damage, κ_{c2} (-)	5.0
Initial internal friction coefficient, μ_0 (-)	0.4
Final internal friction coefficient, μ_∞ (-)	0.0
Transitional normal stress, σ_{N0} (MPa)	600
Densification ratio, E_d/E_0 (-)	1.81

Traditional Column Reinforcement. The baseline reinforcement case was composed of only Grade 60 longitudinal reinforcing bars and stirrups – a relatively standard design in practice. Four 25 mm bars were placed at the corners of the stirrups and oriented in the longitudinal direction for the full length of the column – with complete development in the rigid body section. Closed-loop stirrups 10 mm in diameter were placed at 315 mm spacings for the length of the column, with two stirrups at 200 mm spacings adjacent to each support. The material model parameters used in the numerical simulations for Grade 60 reinforcing bars and stirrups were as follows: density $\rho = 7,800$ kg/m^3, yield strength $\sigma_y = 250$ MPa, ultimate strength $\sigma_u = 400$ MPa, strain at fracture $\bar{\varepsilon}^{pl}_D = 0.18$, stress triaxiality $\eta = 0.333$, and strain rate $\dot{\bar{\varepsilon}}^{pl} = 2.5 \times 10^{-2}$ s^{-1}.

Encased Steel H-Beam Reinforcement. The reinforcement in the steel H-beam case consisted of an ASTM A992 steel W10×60 and all reinforcing bars and stirrups from the 'Traditional Column Reinforcement' case. The W10×60 was oriented with its strong-axis outward, toward the detonation point. As with the reinforcing bars, the H-beam was fully-developed in the rigid body sections. The material model parameters used in the numerical simulations for the A992 steel H-Beam were: density $\rho = 7,850$

Table 3: Values of material model parameters used in numerical simulations for composite H-Beam reinforcement [16]; values with an asterisk were approximated.

Parameter	Value
Longitudinal modulus, E_1 (GPa)	126
Transverse modulus, E_2 (GPa)	11
Major Poisson's ratio, ν_{12} (-)	0.28
Through thickness Poisson's ratio, ν_{23} (-)	0.4
In-plane shear modulus, G_{12} (GPa)	6.6
Transverse shear modulus, G_{23} (GPa)	3.3*
Longitudinal tensile strength, σ_{t1} (MPa)	1,950
Longitudinal compressive strength, σ_{c1} (MPa)	1,480
Transverse tensile strength, σ_{t2} (MPa)	48
Transverse compressive strength, σ_{c2} (MPa)	200
In-plane shear strength, S_{12} (MPa)	79
Transverse shear strength, S_{23} (MPa)	79*
Density, ρ (kg/m^3)	1,600

kg/m^3, Poisson's ratio $\nu = 0.30$, yield strength $\sigma_y = 345$ MPa, ultimate strength $\sigma_u = 450$ MPa, strain at fracture $\bar{\varepsilon}^{pl}_D = 0.20$, stress triaxiality $\eta = 0.333$, and strain rate $\dot{\bar{\varepsilon}}^{pl} = 2.5 \times 10^{-2}$ s^{-1}.

Encased Carbon Fiber Composite H-Beam Reinforcement. The reinforcement in the composite case consisted of a built-up H-beam composed of a laminated carbon fiber AS4 3501-6/epoxy composite, as well as all reinforcing bars and stirrups from the first case. The H-beam cross section was designed to develop the same ultimate bending capacity as the steel H-beam, for a relatively equal static-strength comparison. This resulted in a built-up section with the following geometry: flange width $b_f = 305$ mm, flange thickness $t_f = 17.3$ mm, beam depth $d = 259.6$ mm, and web thickness $t_w = 10.7$ mm. Further, this corresponded to a 16% reduction in total column mass (inclusive of concrete), from the steel H-beam case. The lamina layup used in the numerical simulations was composed of 0.5 mm layers in orientations of 0°, 90°, -45°, 45°, 90°, 0°, 45°, -45° symmetric repeating orientations (center of lamina is immediately after last layer orientation listed). When layer sequences were incompatible with the required plate thickness, repetitions were built out from the center orientation such that the plate layup was always symmetric. Material model parameters for each unidirectional layer of the laminate were derived from AS4 3501-6/epoxy composite data in Soden et al. [16], and are provided in Table 3.

Detonation Loading and Model Execution. Given the magnitude of blast in the near-standoff (severe) case, discrete pressure fields were used rather than the CONWEP model. In the same manner as performed for the validation study, surface elements were employed to apply blast loading. A set of five surface meshes dividing the longitudinal direction were created for each column face to reproduce the vertical pressure gradient. Each of these five surfaces were then tied to a full column face mesh, which was in turn tied to the LDPM nodes on that face. While the incident (front) column face will experience the most significant loading, the rear and side faces will undergo some loading due to ground and structural reflections, and thus this process was applied to each face.

As with the validation study, the column simulations were performed for several times the length of the blast pressure history to capture any inertial effects. For all column cases an explicit dynamic simulation with a time increment less than the critical time increment was selected, and run for a period of 0.02 seconds – six times the duration of the pressure history.

6.2. Evaluation of Column Performance

During simulation, the LDPM nodes falling within the middle 100 mm of the column height were tracked in space for numerical comparison between differing reinforcement strategies. The average displacement of these nodes versus time for the mild and severe pressure cases are provided in Figure 7a and b.

In the mild loading (Figure 7a), all reinforcement strategies displayed an oscillatory pattern for these nodal displacements, which corresponded to free vibrations of the column, mostly in the elastic regime. While all three cases demonstrated this mode of response, there existed a clear hierarchy in level of displacement and energy dissipation. The steel H-beam reinforcement at maximum exhibited 2×10^{-3} m (2 mm) of displacement at center, while the traditionally reinforced case was approximately 3.5×10^{-3} m (3.5 mm). The composite H-beam reinforcement performed at a level in between the other two cases. In addition to the lessened peak displacement, the steel and composite H-beams oscillated at a higher frequency than the traditionally reinforced case, due to increased stiffness.

Under severe loading (Figure 7b), significantly more displacement was experienced for all column designs. The traditionally reinforced case exhibited a steep initial displacement plot, followed by a near linear increasing displacement versus time, corresponding to an approximate free rigid body motion in space due to severe detachment. At the time of simulation end (0.02 seconds, or six times the pressure history), the center of the rebar reinforced column had already traveled over 200 mm. The composite H-beam reinforced column experienced a similar initial steep displacement plot; however, by the time of simulation end, the slope of the displacement curve had plateaued and gone negative, implying complete detachment did not occur and the column was beginning to rebound. In the final steel H-beam reinforcement scenario, significantly less displacement was observed initially and at maximum. At $t = 0.007$ seconds the steel saw a maximum displacement of only 50 mm, and proceeded to rebound twice in the simulation time. While the steel H-beam reinforced column did complete an oscillation, some non-recoverable deformation was observed on the order of 30-40 mm.

To better understand the response, failure mode, and fracture/ejecta of each column, crack openings in the con-

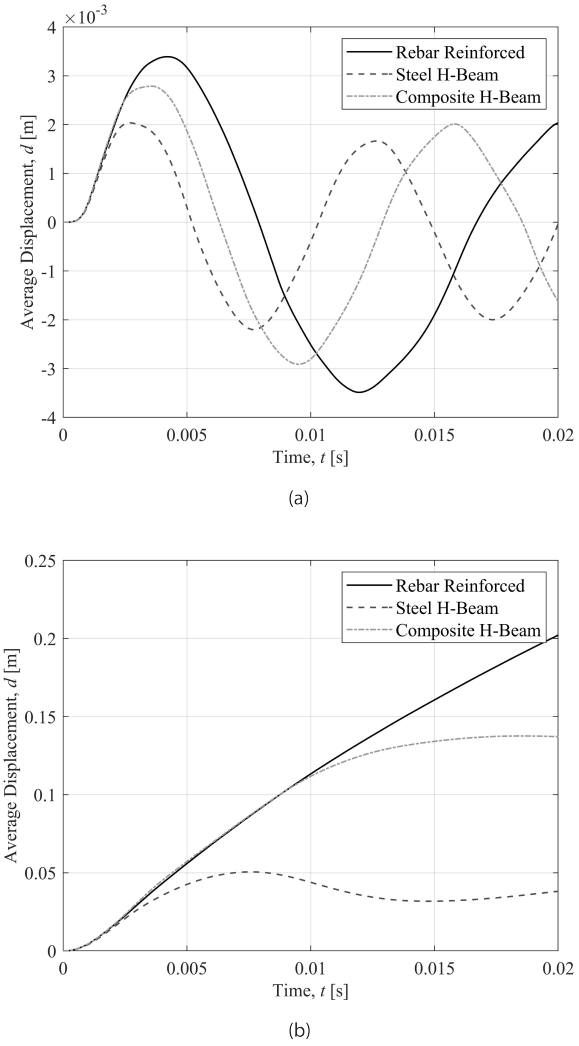

Figure 7: Average displacement of all LDPM nodes falling within the middle 100 mm of the column height versus time for (a) the mild blast case; (b) the severe blast case. Note, both plots are the average of three mesh generation seeds.

crete and principal strain in the reinforcement were examined. Plots of these measures, corresponding to the end of the simulation time, are shown in Figure 8.

As exhibited in the mild loading crack and strain plots (Figure 8a to c), all simulations under the mild pressure level experienced little damage. The columns remained mostly in the elastic regime, and only developed minor hairline cracks. Even the traditionally reinforced case resulted in no cracks larger than 0.005 mm in opening, and no rebar strains greater than 0.5% of the strain at fracture. The steel H-beam reinforced case observed even milder cracking and virtually no measurable strain in the reinforcement. The composite H-beam reinforced case was of similar behavior under this loading, however exhibited slightly greater and larger cracks than the steel H-beam, likely due to the increased composite stiffness and less mass-based energy dissipation.

Under the significantly increased pressure of the severe loading, all columns exhibited some level of structural failure (Figure 8d to f). The traditionally reinforced case, as expected from the displacement plot, observed complete failure of the concrete and reinforcement. This failure was concentrated at the bottom support, the location of maximum loading. The top rebar remained slightly intact; however, with a longer simulation run it is likely this would also disconnect. Regardless of that connection, the column would retain no load bearing capacity. The steel H-beam column performed quite well given the magnitude of loading. Although it experienced significant deflection, none of the steel in the main reinforcing member retained more than 40% of its failure strain at simulation end. While the main reinforcing member remained intact, several stirrups reached failure strains and significant spalling of the concrete at the column rear developed. Both of these factors can greatly reduce residual load capacity, while also creating new and potentially damaging projectiles. The composite H-beam demonstrated resistance between that of the traditional and steel H-beam reinforcement case. Unlike the steel H-beam, the composite H-beam did see some failure within the main reinforcing member, including tearing through about half of the member at the center-height, and minor tearing at the top and bottom near the supports. Further, all four longitudinal bars were completely failed at one or two locations. As with the other H-beam, significant spalling of the concrete occurred at the rear face. While there is likely little residual load capacity in the composite reinforced case, it did not fully disconnect or become a complete projectile like the traditionally reinforced column.

In summary, all three columns under the mild blast loading saw no damage beyond hairline cracking and likely retained most of their original load capacity. All three columns under the severe loading saw significant structural damage; in the traditionally reinforced case the entire column sheared off and would likely become a large projectile; in the steel H-beam case the major reinforcing elements remained intact with some concrete ejecta; in the composite H-beam case all reinforcement was significantly compromised and produced major concrete ejecta.

7. Discussion

Past research activities in conjunction with experimental data demonstrate that LDPM can capture concrete behavior well under high dynamic events such as projectile impacts and minor blast loading. The formulation improvements provided in this paper have extended LDPM to applications of near-field explosives and large detonation events. Further, to streamline simulation of real world structures and structural components for the present practitioner, LDPM has been implemented in the commercial finite element solver Abaqus Unified FEA. As a preliminary check on model fidelity, simulations were performed on experimental conditions and validated with data from Kumar et al. [49]. In the current exercise, the updated

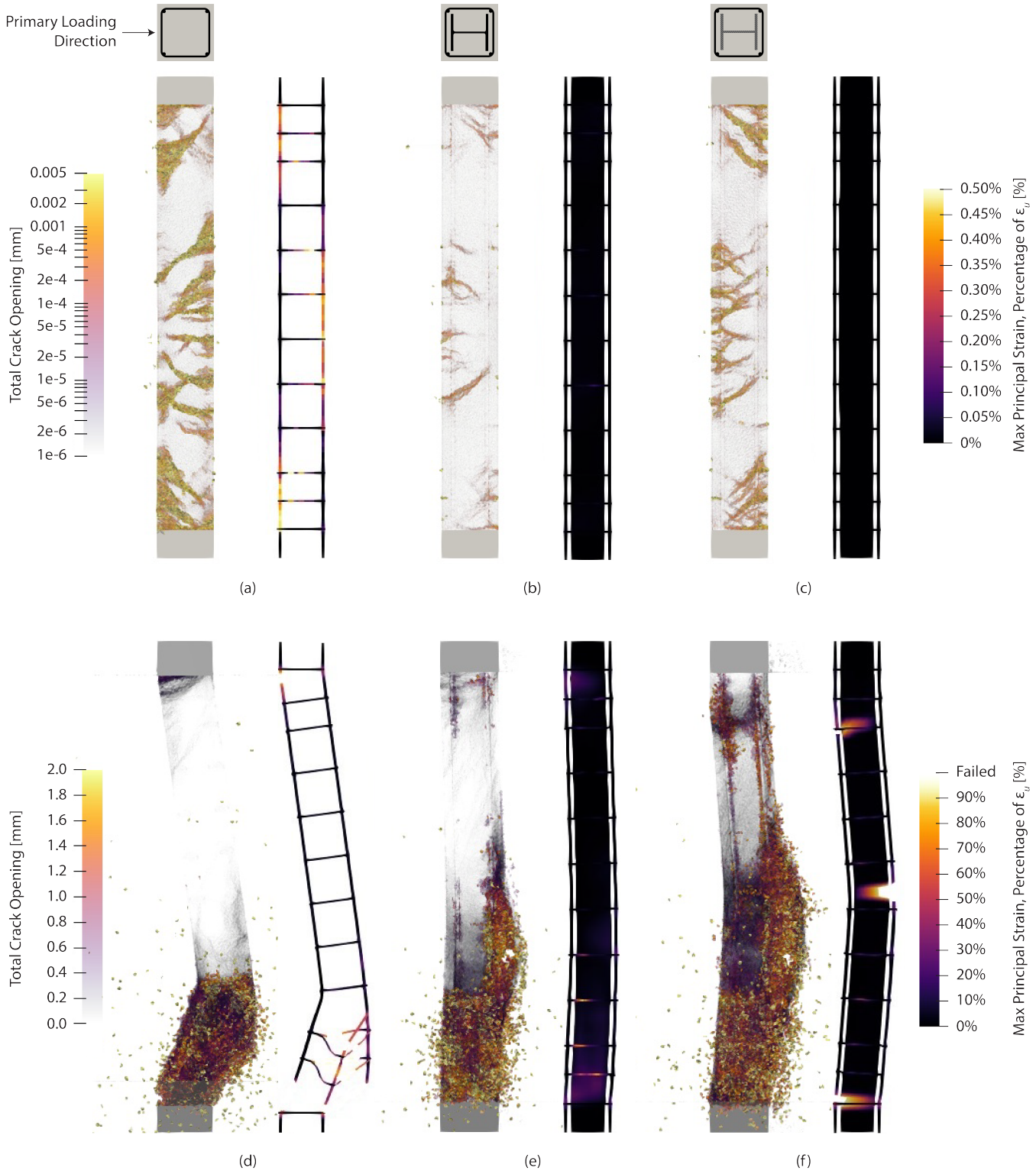

Figure 8: Plot of column crack openings and reinforcement principal strain under mild blast loading for (a) traditional column reinforcement; (b) encased steel H-beam reinforcement; (c) encased carbon fiber composite H-beam. Column crack openings and reinforcement principal strain under severe blast loading for (d) traditional column reinforcement; (e) encased steel H-beam reinforcement; (f) encased carbon fiber composite H-beam. All images are plotted at time $t = 0.02$ seconds, equivalent to $6\times$ the duration of the pressure history.

LDPM formulations and commercial solver implementation performed exceptionally well. Overall behavior such as cracking and blast cones were reproduced, while numerical measures such as blast cone size matched with an average error of less than 5%. One instance of physical phenomena absent from the numerical simulations was the increased blast cone size in the diagonal directions (resulting in a more squared-off cone than truly circular one). This phenomenon was expected to be a cause of overlapping rebar inclusions, and could perhaps be resolved in the future by deliberately including concrete mesh voids at these locations.

As discussed, it is of interest to examine the behavior of concrete reinforced with encased H-beams of steel and composite, as compared to traditional reinforcement, for hazard mitigation due to very large blast loads, such as those associated with vehicle-bourne detonations. To this end, three equally-sized columns were developed with traditional rebar, encased steel H-beam, and encased carbon fiber epoxy composite H-beam reinforcement strategies. The columns were then subjected to mild and severe pressure loads appropriate for such detonations. Overall, the encased beam columns provided greater energy dissipation and damping than their rebar counterparts. In the mild case all three columns experienced virtually no damage, and therefore the most suitable column is likely the one that is most cost effective and meets other project requirements. The severe loading induced significant damage for all columns, with complete failure of the rebar reinforced column. While damage was significant in the H-beam cases, the steel column likely survived with reduced load capacity. It is expected the composite column would retain little axial capacity after such a detonation; however, the reinforcement was sufficient to prevent the column from becoming a projectile, and potentially delaying any subsequent structural failure. Inclusive of concrete, the column with encased composite member saw a total weight reduction of approximately 16% over the column with encased steel. While not a major weight-savings, this design may provide a suitable retrofitting alternative when steel encased members exceed a structure's existing load capacity. In summary, the following conclusions can be made:

1. LDPM remains an appropriate concrete model for highly dynamic events such as blasts.
2. The reformulated LDPM permits simulation of concrete associated with large detonation loadings.
3. When blast loading is within the capacity of traditional reinforcement, the simplest column design is likely the most appropriate.
4. In the event of large blast loads, such as near-field VBIED detonations, columns with encased members provide better structural resistance.
5. Carbon fiber composite reinforcement may be appropriate when weight is of high concern, and when partial structural resilience can be accepted instead of complete structural resistance.

Future work is planned toward implementing a more detailed LDPM facet failure criterion. The current implementation is based on volumetric strain and potentially overestimates failure of facets for particles that are connected to the main structure. For example, if two particles within a tetrahedron detach and fly away, but the other two are still attached to the surface of the concrete member, the current formulation may denote failure of the stationary particles. Additionally, if quality material data can be acquired at the specified strain rates, rate effect will be included in future simulations. Finally, to better quantify true column performance, it is suggested that simulations of these types be followed up with additional simulations to attain the residual axial load capacity in the damaged configuration.

Funding

This work was supported in part by the Naval Sea Systems Command under SBIR Contract No. N6833520C0650; through high-performance computer time and resources from the DoD High Performance Computing Modernization Program; and through the computational resources and staff contributions provided for the Quest high performance computing facility at Northwestern University which is jointly supported by the Office of the Provost, the Office for Research, and Northwestern University Information Technology.

References

[1] N. S. Ha, G. Lu, A review of recent research on bio-inspired structures and materials for energy absorption applications, Composites Part B-engineering 181 (2020) 107496.

[2] F. Xu, X. Zhang, H. Zhang, A review on functionally graded structures and materials for energy absorption, Engineering Structures 171 (2018) 309–325.

[3] J. Zhang, G. Lu, Z. You, Large deformation and energy absorption of additively manufactured auxetic materials and structures: A review, Composites Part B-engineering 201 (2020) 108340.

[4] A. B. M. Supian, S. M. Sapuan, M. Y. M. Zuhri, E. S. Zainudin, H. H. Ya, Hybrid reinforced thermoset polymer composite in energy absorption tube application: a review, Defence Technology 14 (2018) 291–305.

[5] X. Tang, X. Yan, Acoustic energy absorption properties of fibrous materials: A review, Composites Part A-applied Science and Manufacturing 101 (2017) 360–380.

[6] D. Hu, Y. Wang, B. Song, L. Dang, Z. Zhang, Energy-absorption characteristics of a bionic honeycomb tubular nested structure inspired by bamboo under axial crushing, Composites Part B: Engineering (2019).

[7] H. Yang, H. Lei, G. Lu, Z. Zhang, X. Li, Y. Liu, Energy absorption and failure pattern of hybrid composite tubes under quasi-static axial compression, Composites Part B-engineering 198 (2020) 108217.

[8] M. Mohsenizadeh, F. Gasbarri, M. Munther, A. Beheshti, K. Davami, Additively-manufactured lightweight metamaterials for energy absorption, Materials & Design 139 (2018) 521–530.

[9] D. Qi, Q. Lu, C. He, Y. Li, W. Wu, D. Xiao, Impact energy absorption of functionally graded chiral honeycomb structures, Extreme Mechanics Letters (2019).

[10] K. Wu, B. Li, K. C. Tsai, The effects of explosive mass ratio on residual compressive capacity of contact blast damaged composite columns, Journal of Constructional Steel Research 67 (2011) 602–612.
[11] R. Jayasooriya, D. P. Thambiratnam, N. J. Perera, Blast response and safety evaluation of a composite column for use as key element in structural systems, Science & Engineering Faculty (2014).
[12] D.-K. Thai, T.-H. Pham, D.-L. Nguyen, Damage assessment of reinforced concrete columns retrofitted by steel jacket under blast loading, The Structural Design of Tall and Special Buildings (2019).
[13] Z. Wang, H. Wu, J. Wu, Q. Fang, Experimental study on the residual seismic resistance of ultra high performance cementitious composite filled steel tube (UHPCC-FST) after contact explosion, Thin-walled Structures 154 (2020) 106852.
[14] G. Cusatis, A. Beghini, Z. P. Bažant, Spectral stiffness microplane model for quasibrittle composite laminates—Part I: Theory, Journal of Applied Mechanics 75 (2008) 021009.
[15] A. Beghini, G. Cusatis, Z. P. Bažant, Spectral stiffness microplane model for quasibrittle composite laminates—Part II: Calibration and validation, Journal of Applied Mechanics 75 (2008) 021010.
[16] P. D. Soden, M. J. Hinton, A. S. Kaddour, Lamina properties, lay-up configurations and loading conditions for a range of fibre-reinforced composite laminates, Composites Science and Technology 58 (1998) 1011–1022.
[17] Standard Specification for Steel for Structural Shapes For Use in Building Framing, Standard, ASTM International, West Conshohocken, PA (Aug. 2017).
[18] National Academy of Engineering, IED attack improvised explosive devices, A fact sheet from the National Academies and the Department of Homeland Security (2019).
[19] U.S. Fire Administration, The world trade center bombing: Report and analysis USFA-TR-076, Technical Report Series (1993).
[20] Office of the Inspector General, An investigation of the belated production of documents in the oklahoma city bombing case, Special Report (2002).
[21] Federal Emergency Management Agency, Reference manual to mitigate potential terrorist attacks against buildings, FEMA 426, Risk Management Series (2003).
[22] R. Bergema, O. Kearney, An analysis of the democratization of the terrorist threat in the west, International Centre for Counter-Terrorism Report (2020).
[23] National Consortium for the Study of Terrorism and Responses to Terrorism , Comparing failed, foiled, completed and successful terrorist attacks: Year 5 final report, Report to the Office of University Programs, Science and Technology Directorate, U.S. Department of Homeland Security (2017).
[24] T. Bjørgo, A. R. Jupskås, The long-term impacts of attacks: The case of the July 22, 2011 attacks in Norway, Perspectives on Terrorism (2021).
[25] Cybersecurity & Infrastructure Security Agency, Vehicle ramming, security awareness for soft targets and crowded places, Action Guide (2018).
[26] S. E. Rigby, A. Tyas, T. Bennett, S. Clarke, S. D. Fay, The negative phase of the blast load, International Journal of Protective Structures 5 (2014) 1 – 19.
[27] H. Jin, H. Hao, Y. Hao, W. Chen, Predicting the response of locally resonant concrete structure under blast load, Construction and Building Materials 252 (2020) 118920.
[28] G. Cusatis, D. Pelessone, A. Mencarelli, Lattice discrete particle model (LDPM) for failure behavior of concrete. I: Theory, Cement and Concrete Composites 33 (9) (2011) 881–890.
[29] G. Cusatis, A. Mencarelli, D. Pelessone, J. Baylot, Lattice discrete particle model (LDPM) for failure behavior of concrete. II: Calibration and validation, Cement and Concrete composites 33 (9) (2011) 891–905.
[30] G. Cusatis, Z. P. Bažant, L. Cedolin, Confinement-shear lattice model for concrete damage in tension and compression: I. theory, Journal of Engineering Mechanics 129 (12) (2003) 1439–1448.
[31] G. Cusatis, Z. P. Bažant, L. Cedolin, Confinement-shear lattice CSL model for fracture propagation in concrete, Computer methods in applied mechanics and engineering 195 (52) (2006) 7154–7171.
[32] G. Cusatis, L. Cedolin, Two-scale study of concrete fracturing behavior, Engineering Fracture Mechanics 74 (1-2) (2007) 3–17.
[33] L. Wan-Wendner, R. Wan-Wendner, G. Cusatis, Age-dependent size effect and fracture characteristics of ultra-high performance concrete, Cement and Concrete Composites 85 (2018) 67–82.
[34] M. Alnaggar, D. Pelessone, G. Cusatis, Lattice discrete particle modeling of reinforced concrete flexural behavior, Journal of Structural Engineering 145 (1) (2019) 04018231.
[35] C. Ceccato, M. Salviato, C. Pellegrino, G. Cusatis, Simulation of concrete failure and fiber reinforced polymer fracture in confined columns with different cross sectional shape, International Journal of Solids and Structures 108 (2017) 216–229.
[36] R. Rezakhani, G. Cusatis, Asymptotic expansion homogenization of discrete fine-scale models with rotational degrees of freedom for the simulation of quasi-brittle materials, Journal of the Mechanics and Physics of Solids 88 (2016) 320–345.
[37] J. Smith, G. Cusatis, Numerical analysis of projectile penetration and perforation of plain and fiber reinforced concrete slabs, International Journal for Numerical and Analytical Methods in Geomechanics 41 (3) (2017) 315–337.
[38] G. Cusatis, Strain-rate effects on concrete behavior, International Journal of Impact Engineering 38 (4) (2011) 162–170.
[39] J. Smith, G. Cusatis, D. Pelessone, E. Landis, J. O'Daniel, J. Baylot, Discrete modeling of ultra-high-performance concrete with application to projectile penetration, International Journal of Impact Engineering 65 (2014) 13–32.
[40] J. Feng, M. Song, Q. He, W. Sun, L. Wang, K. Luo, Numerical study on the hard projectile perforation on RC panels with LDPM, Construction and Building Materials (2018).
[41] M. Smith, ABAQUS/Standard User's Manual, Version 2017, Dassault Systèmes Simulia Corp, United States, 2017.
[42] G. Cusatis, X. Zhou, High-order microplane theory for quasibrittle materials with multiple characteristic lengths, Journal of Engineering Mechanics-ASCE 140 (2014) 04014046.
[43] S. J. Green, S. R. Swanson, Static constitutive relations for concrete, 1973.
[44] Dassault Systèmes, Abaqus Unified FEA (2017).
URL `https://www.3ds.com/products-services/simulia/products/abaqus/`
[45] M. Troemner, E. Ramyar, G. Cusatis, Poly-material lattice discrete particle model for the multiscale prediction of elastic properties of concrete (Manuscript in preparation).
[46] M. Alnaggar, D. Pelessone, G. Cusatis, Lattice discrete particle modeling (LDPM) of flexural size effect in over reinforced concrete beams, 2016.
[47] Design & Analysis of Hardened Structures to Conventional Weapons Effects, Standard, United States Army, The Pentagon; Arlington County, Virginia, U.S (Nov. 1986).
[48] D.E. Hyde, CONWEP, Conventional Weapons Effects Program (1992).
[49] V. Kumar, K. Kartik, M. Iqbal, Experimental and numerical investigation of reinforced concrete slabs under blast loading, Engineering Structures 206 (2020) 110125.